Research Square

Preprints are preliminary reports that have not undergone peer review.
They should not be considered conclusive, used to inform clinical practice,
or referenced by the media as validated information.

NK cells initiate an IFN-γ–dependent innate-to-adaptive immune cascade driving antitumor immunity upon ferroptosis induction

Lingyu Li
lilingyu@jlu.edu.cn

The First Hospital, Jilin University
Yongfei Zhang
The First Hospital, Jilin University
Yingnan Cui
The First Hospital, Jilin University
Yantong Guo
The First Hospital, Jilin University
Jinjin Zhang
The First Hospital, Jilin University
Yuhong Lei
The First Hospital, Jilin University
Jingyun Chen
The First Hospital, Jilin University
Zhihuan Qu
The First Hospital, Jilin University
Yufeng Wang
First Hospital of Jilin University,

Article

Keywords:

Posted Date: April 2nd, 2026

DOI: https://doi.org/10.21203/rs.3.rs-9229089/v1

License: This work is licensed under a Creative Commons Attribution 4.0 International License.
Read Full License

Additional Declarations: There is **NO** Competing Interest.

Abstract

Ferroptosis has been widely viewed as a downstream effector mechanism amplified by adaptive immunity. Here, we redefine ferroptosis as an immune-initiating event by demonstrating that GPX4 inhibition engages natural killer (NK) cells as essential upstream regulators. Mechanistically, early IFN-γ derived from NK cells provides a critical permissive signal that promotes dendritic cell maturation and primes subsequent $CD8^+$ T cell responses, thereby establishing a functional innate–adaptive immune axis. Disruption of this NK cell–dependent circuit, such as in obese hosts, impairs ferroptosis-associated antitumor immunity and confers resistance to GPX4-targeted therapy. Notably, therapeutic activation of NK cells with IL-15 restores this immune–ferroptosis axis and overcomes treatment resistance. Together, our findings establish a cellular hierarchy in ferroptosis-associated immunity, identify NK cells as critical initiators of ferroptosis-driven antitumor responses, and provide a mechanistic rationale for combinatorial strategies to enhance ferroptosis-based cancer therapy.

Introduction

Ferroptosis is a form of regulated cell death characterized by iron-dependent lipid peroxidation and has emerged as a promising therapeutic target in cancer [1-5]. Inhibition of glutathione peroxidase 4 (GPX4), a key enzyme that detoxifies lipid hydroperoxides, disrupts the cellular defense system against oxidative damage and effectively induces ferroptosis in tumor cells, leading to potent antitumor effects in multiple preclinical models [6-9]. Beyond its direct cytotoxic activity, accumulating evidence suggests that ferroptosis can also remodel the tumor immune microenvironment through the release of immunogenic signals, pointing to an important immunomodulatory role [10-12].

Seminal work by Wang et al., published in Nature, revealed that interferon-γ (IFN-γ) derived from activated $CD8^+$ T cells promotes ferroptosis by downregulating the cystine/glutamate antiporter system xc^-, thereby suppressing antioxidant capacity in tumor cells [10], positioning adaptive immunity as a critical amplification mechanism that enhances ferroptosis execution. However, because $CD8^+$ T cell activation requires antigen presentation and clonal expansion—a process that typically takes several days—this paradigm does not explain how ferroptosis execution is initially enabled *in vivo* during the early phase following GPX4 inhibition, before adaptive immunity is fully established. This temporal gap raises the possibility that innate immune–derived signals may provide the initial permissive cues that enable ferroptosis execution and subsequent immune amplification.

Natural killer (NK) cells are key effectors of innate immunity that function as immunological sentinels. They reside within tissues, including the tumor microenvironment, and are poised to rapidly respond to cellular stress and damage signals [13-15]. NK cells are also an early source of IFN-γ and play a critical bridging role in promoting dendritic cell (DC) maturation and subsequent $CD8^+$ T cell activation [16, 17]. However, whether NK cells serve as initiating regulators of ferroptosis-induced antitumor immunity has remained unknown.

Here we show that GPX4 inhibition preferentially activates NK cells, which are essential for the subsequent establishment of $CD8^+$ T cell responses. Mechanistically, basal IFN-γ derived from NK cells provides a permissive signal that enables ferroptosis execution in GPX4-inhibited tumor cells, even in the presence of exogenous vitamin E. These findings identify NK cells as key initiators of ferroptosis-induced anti-tumor immunity, provide mechanistic insights into ferroptosis resistance in immunosuppressive conditions, and establish a rationale for combination therapies targeting the GPX4-NK-IFN-γ axis.

Results

GPX4 inhibition triggers tumor ferroptosis and promotes anti-tumor immunity in vivo

To investigate whether targeting GPX4 effectively induces ferroptosis *in vivo* and influences the tumor immune microenvironment (Fig. 1a), we first generated GPX4-knockout B16 melanoma cell lines using CRISPR-Cas9 (sgGPX4). In parallel, wild-type B16 cells were treated with withaferin A (WFA), which suppresses *GPX4* gene expression [6], or N6F11, which promotes GPX4 protein degradation [18], thereby downregulating GPX4 through complementary pharmacological strategies (Fig. 1b; Supplementary Fig. 1A-B).

C57BL/6 mice were subcutaneously implanted with sgNC (control) or sgGPX4 B16 cells, or treated with WFA or N6F11 after establishment of B16 tumors. Tumors were harvested 14 days post-inoculation to assess lipid reactive oxygen species (ROS) accumulation (Fig. 1a). Both genetic ablation and pharmacological inhibition of GPX4 resulted in a marked increase in lipid ROS levels within tumor cells (Fig. 1c), consistent with induction of ferroptosis *invivo*. Consistently, GPX4 depletion or inhibition significantly suppressed B16 tumor growth, an effect that was largely abolished by the ferroptosis inhibitor liproxstatin-1 (Lip-1) [18, 19] (Fig. 1d-f; Supplementary Fig. 1C-D), supporting that the observed tumor growth suppression is ferroptosis-dependent.

We next examined the impact of GPX4 targeting on the tumor immune microenvironment. Consistent with previous reports [7, 11, 12, 20] , flow cytometric analysis showed that GPX4 knockout was associated with a marked increase in the frequency of tumor-infiltrating $CD8^+$T (TIL-$CD8^+$T) cells and NK (TIL-NK) cells (Fig. 1g). These immune populations also displayed enhanced effector phenotypes, including increased production of IFN-γ and TNF-α, as well as elevated expression of granzyme B (GZMB) (Fig. 1h-i). Similar immunological alterations were observed in tumors treated with N6F11 (Supplementary Fig. 1E-G).

Collectively, these findings confirm that genetic and pharmacological targeting of GPX4 induces ferroptosis *in vivo* and is associated with enhanced infiltration and activation of cytotoxic lymphocytes, consistent with induction of antitumor immune responses.

GPX4 inhibition requires NK cell–dependent immunity for tumor suppression in vivo

To determine whether the *in vivo* tumor suppression mediated by GPX4 targeting depends on the host immune system, we established tumor models with either genetic GPX4 knockout or pharmacological inhibition in immunocompetent C57BL/6 mice and severely immunodeficient NCG mice. All three GPX4-targeting strategies robustly suppressed tumor growth in C57BL/6 mice; however, this antitumor effect was largely abolished in NCG mice (Fig. 2a-b, Supplementary Fig. 2A-C), indicating that an intact immune system is required for the full antitumor efficacy of GPX4 inhibition.

Previous studies have shown that IFN-γ produced by cytotoxic immune cells can enhance tumor cell sensitivity to ferroptosis by downregulating system Xc^- [10, 21]. To assess whether IFN-γ contributes to GPX4 inhibition–mediated tumor suppression, we subcutaneously implanted sgNC or sg*GPX4* B16 cells into wild-type (WT) or *Ifng*$^{-/-}$ mice (Supplementary Fig. 2D) and evaluated intratumoral lipid ROS levels and tumor growth. While GPX4 knockout led to a marked increase in lipid ROS accumulation and tumor growth inhibition in WT mice, both effects were largely reversed in *Ifng*$^{-/-}$ mice (Fig. 2c-d). Similar results were observed in WFA-treated tumors (Fig. 2e-f), supporting a functional requirement for IFN-γ in mediating the full ferroptotic and antitumor effects of GPX4 inhibition *in vivo*.

As both NK cells and $CD8^+$ T cells represent major sources of IFN-γ within tumors [22, 23], we next sought to define the relative contribution of these cell populations. To this end, we employed $CD8^+$ T cell-deficient mice (*Cd8a*$^{cre+/}$ *Lck*$^{fl/fl}$; Supplementary Fig. 2E) and antibody-mediated NK cell depletion (anti-NK1.1; Supplementary Fig. 2F) in GPX4 knockout or pharmacological inhibition models. Compared with *Lck*$^{fl/fl}$ control mice, GPX4 inhibition–mediated tumor growth suppression was only partially attenuated in $CD8^+$ T cell-deficient mice (Fig. 2g-h). In contrast, depletion of NK cells completely abrogated the antitumor effect of GPX4 targeting (Fig. 2i-j). These results indicate that NK cells play a dominant role in mediating tumor control following GPX4 inhibition, whereas $CD8^+$ T cells contribute to this effect but are not solely sufficient.

NK cell depletion abolishes GPX4 inhibition–induced CD8⁺ T cell activation

To further delineate the role of NK cells in GPX4 targeting-mediated immune activation, we performed flow cytometric analyses of tumor tissues collected at day 3 and day 10 following WFA treatment in the B16 tumor model (Fig. 3a). At an early time point (day 3), GPX4 inhibition led to a pronounced increase in both the abundance and activation status of TIL-NK cells, indicating that NK cells rapidly sense and respond to the ferroptotic tumor microenvironment. (Fig. 3b-c). In contrast, no significant changes in $CD8^+$ T cell infiltration or activation were observed at this early stage (Fig. 3b, d). By day 10 after treatment, however, TIL-$CD8^+$ T cells displayed a marked increase in both frequency and effector function, acquiring an activation profile comparable to that observed for TIL-NK cells (Fig. 3e-g). These observations suggest that NK cell activation precedes $CD8^+$ T cell activation following GPX4 inhibition.

We next examined whether NK cells are required for the subsequent activation of $CD8^+$ T cells following GPX4 targeting. Mice were treated with anti-NK1.1 or control IgG antibodies prior to WFA administration, and TIL-$CD8^+$ T cells were analyzed on day 10. Notably, depletion of NK cells completely abrogated the

WFA-induced increase in both $CD8^+$ T cell infiltration and effector activation (Fig. 3h-i). To corroborate these results in an independent genetic model, we compared GPX4-knockout and wild-type B16 tumors. Mice received anti-NK1.1 or IgG antibodies beginning on the day 1 of tumor inoculation, and tumors were analyzed on day 14. Consistently, the enhanced infiltration and activation of $CD8^+$ T cells observed in GPX4-deficient tumors were fully reversed upon NK cell depletion (Fig. 3j-k). Collectively, these data indicate that NK cells are required for optimal $CD8^+$ T cell activation following GPX4 inhibition.

NK cell-derived IFN-γ orchestrates dendritic cell activation and adaptive immune priming in response to GPX4 inhibition

Given our earlier observation that IFN-γ expression in TIL-NK cells is markedly elevated at early stages of GPX4-targeted therapy, and considering the established immunoregulatory role of NK cell-derived IFN-γ in shaping adaptive immune responses, particularly $CD8^+$ T cell immunity [17, 24, 25], we generated NK cell-specific IFN-γ conditional knockout mice ($Ifng^{\Delta NK}$), with $Ifng^{fl/fl}$ littermates serving as controls (Fig. 4a-b). Following subcutaneous implantation of B16 tumors, mice were treated with WFA, and tumor growth, intratumoral lipid ROS, and immune microenvironmental changes were analyzed on day 10 (Fig. 4c).

ELISA analysis revealed reduced basal IFN-γ levels in both peripheral blood and tumor tissues of $Ifng^{\Delta NK}$ mice. While WFA treatment induced a robust increase in intratumoral IFN-γ levels in $Ifng^{fl/fl}$ mice, this induction was completely absent in $Ifng^{\Delta NK}$ mice (Fig. 4d-e), indicating that NK cells represent a major source of therapy-induced IFN-γ following GPX4 inhibition.

Correspondingly, the pronounced tumor growth inhibition observed in WFA-treated $Ifng^{fl/fl}$ mice was entirely lost in $Ifng^{\Delta NK}$ mice (Fig. 4f). Consistent with this finding, WFA failed to induce lipid ROS accumulation within tumors of $Ifng^{\Delta NK}$ mice (Fig. 4g). Moreover, WFA-induced increases in overall immune cell infiltration, as well as the enhanced infiltration and effector activation of $CD8^+$ T cells, were completely abolished in the absence of NK cell-derived IFN-γ (Fig. 4h-i). To exclude potential off-target effects of pharmacological inhibition, these observations were independently validated using GPX4-knockout versus wild-type B16 tumor models, yielding comparable results (Supplementary Fig. 3). Collectively, these data establish NK cell-derived IFN-γ as an essential mediator of GPX4 inhibition-induced ferroptosis and the ensuing antitumor immune response.

Given the central role of dendritic cells (DCs) in linking innate and adaptive immunity, we next investigated whether NK cell-derived IFN-γ regulates DC activation within tumor-draining lymph nodes (dLNs) following GPX4 inhibition. Flow cytometric analysis demonstrated that WFA treatment significantly increased the abundance of $MHCII^+CD11c^+$ DCs in dLNs (Fig. 4j), accompanied by elevated expression of the costimulatory molecules CD80 and CD86 (Fig. 4k). Notably, this WFA-induced expansion and activation of dLN DCs was completely abrogated in $Ifng^{\Delta NK}$ mice, indicating that NK cell-derived IFN-γ is required for DC activation in response to GPX4 targeting (Fig. 4j-k). These findings indicate that NK-derived IFN-γ is required for dendritic cell activation and subsequent $CD8^+$ T cell responses following GPX4 inhibition.

Restoring NK cell function overcomes obesity-associated resistance to GPX4 inhibition-driven tumor ferroptosis and immunity

Given that impaired NK cell function in obesity-particularly diminished IFN-γ secretion-has been widely reported [26], we first established a diet-induced obesity (DIO) mouse model by feeding the mice high-fat diet (HFD) (Supplementary Fig. 4A), accompanied by a marked reduction in IFN-γ production by NK cells (Supplementary Fig. 4B). Because our study demonstrates that the ferroptosis-immune synergy elicited by GPX4-targeted therapy critically depends on NK cell-derived IFN-γ, we hypothesized that obesity-associated NK cell dysfunction may limit the antitumor efficacy of ferroptosis-based therapy in obese hosts.

Based on this rationale, we next tested whether restoring NK cell activity could rescue the immune response to GPX4-targeted therapy under obese conditions. IL-15 and its superagonist analogs, such as ALT-803 [27, 28], are known to potently promote NK cell expansion, survival, and IFN-γ production, and have shown robust immunostimulatory activity in both preclinical and clinical settings. We therefore evaluated the therapeutic efficacy of combining GPX4 inhibitors (WFA or N6F11) with the IL-15 analog ALT-803 in an obese tumor model (Fig. 5a).

Whereas treatment with WFA or N6F11 alone exerted only modest antitumor effects in DIO mice, combination therapy with ALT-803 resulted in pronounced suppression of B16 tumor growth (Fig. 5b). Tumors harvested on day 14 after inoculation showed significantly elevated intratumoral IFN-γ levels in the combination group compared with either monotherapy (Fig. 5c), accompanied by a marked increase in lipid ROS accumulation in tumor cells (Fig. 5d). Consistently, immune profiling revealed that the combination therapy substantially enhanced the infiltration and activation of both tumor-infiltrating NK cells and $CD8^+$ T cells (Fig. 5e-g). In parallel, dendritic cell abundance and the expression of the costimulatory molecules CD80 and CD86 were significantly increased in tumor-draining lymph nodes (Fig. 5h-i).

These findings indicate that restoring NK cell function improves ferroptosis-associated antitumor immunity in obese hosts.

Discussion

This study reveals a ferroptosis-initiated, NK cell–driven innate–adaptive immune regulatory axis and establishes NK cells as the critical initiating regulators of ferroptosis-associated antitumor immunity, thereby expanding and refining the current framework of immune–ferroptosis interactions.

Previous studies demonstrated that $CD8^+$ T cell–derived IFN-γ promotes tumor ferroptosis by suppressing system xc^-, positioning adaptive immunity as a key amplification component of ferroptosis regulation [10, 21]. However, this model primarily addresses how adaptive immunity enhances ferroptosis, while the mechanisms governing the initial triggering of ferroptosis-associated immune responses *in vivo* have remained unclear. Through genetic and immune cell depletion approaches, our study

demonstrates that, in the context of GPX4 inhibition, NK cell activation not only precedes $CD8^+$ T cell responses but is also required for the establishment of functional $CD8^+$ T cell immunity. NK cell depletion completely abolished $CD8^+$ T cell infiltration and effector function acquisition, indicating that NK cells function not merely as early effectors but as essential regulators of adaptive immune priming in ferroptosis-driven antitumor responses.

A central question that arises is how ferroptosis is initially triggered *in vivo* following GPX4 inhibition. Previous studies have proposed that GPX4 loss renders tumor cells ferroptosis-prone [4]; however, lipid-soluble antioxidant systems, particularly vitamin E, can effectively suppress lipid peroxidation chain reactions and prevent ferroptosis execution [29, 30]. To independently assess the role of the immune system in ferroptosis execution under conditions that prevent spontaneous cell death, we supplemented Trolox in vitro and maintained mice on a standard vitamin E-containing diet *in vivo* [12, 31]. Notably, recent work demonstrated that tumor cells acquire α-tocopherol through uptake of circulating lipoproteins, thereby resisting ferroptosis induced by GPX4 deletion [31]. Within this experimental framework, we observed that GPX4-deficient tumors still exhibited significant lipid ROS accumulation and growth suppression in immunocompetent hosts despite sufficient vitamin E availability, whereas these effects were completely absent in IFN-γ–deficient or immunodeficient hosts. These findings indicate that GPX4 inhibition establishes a ferroptosis-prone state, while immune-derived IFN-γ serves as a critical determinant for effective ferroptosis execution. Furthermore, these results suggest that immune-derived signals can overcome antioxidant protection *in vivo* and drive ferroptotic tumor suppression.

Further investigation into the origin and function of this IFN-γ signal suggests that basal IFN-γ produced by NK cells within the tumor microenvironment may play an important role in maintaining tumor cell susceptibility to ferroptosis. As tissue-resident innate immune cells, NK cells constitutively produce low levels of IFN-γ [32], and previous studies have shown that IFN-γ promotes ferroptosis by suppressing system xc^- activity and modulating lipid metabolic pathways [33]. Under conditions of GPX4 inhibition, this persistent immune-derived oxidative pressure may facilitate further lipid ROS accumulation, enabling tumor cells to surpass the ferroptotic threshold. In contrast, in the absence of IFN-γ signaling, antioxidant systems such as vitamin E may be sufficient to maintain tumor cell survival. This model explains why GPX4-deficient tumors remain viable in immunodeficient hosts but undergo ferroptosis-associated growth suppression in immunocompetent settings.

Our temporal kinetic analyses further support the initiating role of NK cells in this process. NK cells were activated early following GPX4 inhibition, whereas $CD8^+$ T cell responses emerged significantly later, consistent with the established role of NK cells as innate immune sentinels [17, 34]. Unlike $CD8^+$ T cells, which require antigen presentation and clonal expansion, NK cells can rapidly respond to tissue damage signals. Ferroptotic tumor cells release damage-associated molecular patterns and oxidized lipid species that promote NK cell activation and IFN-γ production [35, 36]. Once this initial IFN-γ signal is established, the system enters a self-amplifying immune–ferroptosis feedback loop. NK cell–derived IFN-γ promotes ferroptosis execution and enhances dendritic cell maturation, enabling dendritic cells to

prime CD8⁺ T cells in tumor-draining lymph nodes. Activated CD8⁺ T cells subsequently produce large amounts of IFN-γ, further amplifying ferroptosis and antitumor immunity. This sequential process explains the NK cell–dependent establishment of CD8⁺ T cell responses observed in our study and identifies NK cells as critical initiators linking ferroptosis to adaptive immune activation.

Importantly, our findings complement rather than contradict previous studies. While prior work demonstrated that CD8⁺ T cell–derived IFN-γ amplifies ferroptosis-mediated antitumor immunity, our study identifies NK cell–derived IFN-γ as a key permissive signal during the initiation phase. Together, these findings support a unified model in which GPX4 inhibition establishes ferroptosis susceptibility, NK cell–derived IFN-γ enables ferroptosis execution, and CD8⁺ T cell–derived IFN-γ further amplifies this response.

This model also provides mechanistic insight into ferroptosis resistance under immunosuppressive conditions. For example, in obesity, impaired NK cell function and reduced IFN-γ production [26] may limit ferroptosis execution and antitumor immunity, whereas restoration of NK cell function may re-establish this immune–ferroptosis axis and enhance therapeutic efficacy.

Several limitations should be acknowledged. First, our mechanistic studies were primarily conducted in a single tumor model, and further validation across additional tumor types is warranted. Second, the precise molecular mechanisms by which IFN-γ overcomes antioxidant protection and regulates ferroptosis thresholds remain to be fully elucidated.

In summary, our study identifies NK cells and NK-derived IFN-γ as critical regulators of ferroptosis-driven antitumor immunity and establishes a comprehensive immune–ferroptosis regulatory framework in which NK cells initiate and adaptive immunity amplifies ferroptotic responses. These findings provide a conceptual foundation for therapeutic strategies targeting the GPX4–NK–IFN-γ axis to enhance cancer immunotherapy.

Materials and Methods

Cell lines and cell culture

B16F0(B16), HEK293T, CT26, MC38 cells were purchased from ATCC. B16 cells and CT26 cells were cultured in Roswell Park Memorial Institute 1640 medium (RPMI 1640) containing 10% fetal bovine serum (FBS, CellMax) and 100 IU penicillin and 100mg/mL streptomycin. HEK293T and MC38 cells were cultured in Dulbecco's modified Eagle medium (DMEM) containing 10% fetal bovine serum and 100 IU penicillin and 100mg/mL streptomycin. All cells were cultured in a humidified 5% CO_2 atmosphere.

CRISPR-Cas9 mediated GPX4 knockout

GPX4 knockout cells were generated with CRISPR-Cas9 technology. The LentiCRISPRv2 vector plasmid containing guide RNA sequence CGTGTGCATCGTCACCAACG targeting mouse *Gpx4* and packaging

plasmids (pspax2, pMD2.G) were transfected into HEK293T cells using JetPrime transfection reagent, and the medium was replaced the next day. 48 hours post-transfection, the virus supernatant was collected. B16 and MC38 cells were transduced with the virus supernatant and then selected with puromycin. 24 hours post-transfection, monoclonal screening and culture were performed in the presence of 0.2 mM Trolox (MCE, #567834) to maintain the viability of GPX4 knockout tumor cells [29, 30]. After colony formation and expansion, Western blotting was conducted to screen for GPX4 knockout clones.

Animal models

Female C57BL/6 mice (6-8 weeks old) and male C57BL/6 mice (4 weeks old) were purchased from Charles River Laboratories (Beijing, China). Female NCG mice (6-8weeks old) were purchased from GemPharmatech (Nanjing, China). *Lck*$^{fl/fl}$ mice, *Cd8a*$^{cre+/-}$ mice, *Ifng*$^{fl/fl}$ mice, *Ncr1*$^{cre+/-}$ mice, *Ifng*$^{-/-}$ mice were purchased from Cyagen Biosciences (Suzhou, China). All mice were housed in an Specific-Pathogen-Free animal facility and acclimated for one week before the experiment. All animal experiments were approved by the Animal Ethics Committee of the First Hospital of Jilin University.

All mice were fed a diet containing vitamin E (60 IU/kg). For DIO mice model, four-week-old male C57BL/6 mice were fed either high fat diet (HFD)(60% energy from fat, XTHF60,Jiangsu-Xietong,Inc,China) or control diet (CD)(10% energy from fat, Jiangsu-Xietong, Inc, China) for 10 weeks. Body weight was measured every two weeks. After 10 weeks, animal studies were performed.

For subcutaneous tumor model, B16, B16-GPX4^{KO}(2×10^5 cells/mouse), MC38, MC38-GPX4^{KO}(4×10^5 cells/mouse), CT26(2×10^5 cells/mouse) were implanted in the right blank of C57BL/6 mice, *Lck*$^{fl/fl}$ mice *Cd8a*$^{cre+/}$*Lck*$^{fl/fl}$ mice, *Ifng*$^{fl/fl}$ mice *Ifng*$^{\triangle NK}$ mice, Balb/c mice, DIO mice, respectively. B16, B16-GPX4^{KO}(1×10^5 cells/mouse), MC38, MC38-GPX4^{KO}(2×10^5 cells/mouse) were implanted in the right blank of NCG mice, respectively. After tumor implantation, once tumors were detectable or palpable, the length (L) and the width(W) were measured every other day, and the tumor volume (V) was calculated as V= (L×W^2)/2. Mice were randomly assigned to specific groups at the start of the treatment, and euthanized at designated time points, tumor or other organs were collected for subsequent experiments.

For NK cell depletion, anti-NK1.1 antibody (BioXCell, #BE0036) or isotype control anti-IgG (BioXCell, #BE0085) were injected intraperitoneally (i.p.)(300μg/mouse) on day 1-3 after tumor inoculation (day0), then twice one week thereafter.

For administration studies *in vivo*, WFA (MCE, #248596) and N6F11(MCE, #456386) or vehicle were administered starting on day4 post-tumor inoculation. WFA (4mg/kg) was given intraperitoneally once every other day, and N6F11 (10mg/kg) was given intraperitoneally once every 3 days. Lip-1(MCE, #818854) was administered starting on day 1 post-tumor inoculation at a dose of 10 mg/kg once daily via i.p.. ALT-803 (MCE, #875450) was administered starting on day 1 post-tumor inoculation at a dose of 200 μg/kg twice a week via subcutaneous injection.

Quantitative real-time PCR(qRT-PCR)

RNA was extracted using Trizol (Sigma), and reverse transcription was performed with Prime Script™ RT Master Mix. qRT-PCR analysis was conducted using SYBR Green on a CFX96 real-time system (Bio-Rad). The results were normalized to GAPDH mRNA. The primer pairs used were as follows: mouse *GPX4*:forward 5'- TGTGCATCCCGCGATGATT, reverse 5'- CCCTGTACTTATCCAGGCAGA; mouse *GAPDH*:forward 5'- TGTGTCCGTCGTGGATCTGA, reverse 5'- TTGCTGTTGAAGTCGCAGGAG.

Flow cytometry analysis(FACS)

To quantify immune cell and cytokine expression in mice, single-cell suspensions were prepared from fresh tumor tissues, spleens, or lymph nodes. For surface staining, cells were incubated with antibodies against membrane surface markers for 20 minutes. For intracellular staining, the single-cell suspensions were first incubated in medium containing PMA, Ionomycin, and Brefeldin A at 37°C for 4 hours, followed by surface staining with membrane antibodies. The cells were washed, then fixed and permeabilized using the Foxp3/Transcription Factor Fixation/Permeabilization Kit (Invitrogen,#3052352) incubated overnight at 4°C. After washing with Perm/Wash buffer, the cells were stained with cytokine antibodies for 30 minutes and then washed. All samples were acquired on an LSRII flow cytometer (BD Biosciences). The antibodies used in this study include:BV510 anti-CD45 (BioLegend, #103138), APCcy7 anti-CD3 (BioLegend, #100222), PEcy7 anti-CD8 (BioLegend, #100722), APC anti-NKp46 (BioLegend, #137608), FITC anti-CD11c (BioLegend, #117306), PEcy5 anti-MHCII (BioLegend, #107612), PE anti-CD80 (BioLegend, #104708), BV605 anti-CD86 (BioLegend, #105125), PE anti-IFN-γ (BioLegend, #505808), PerCPcy5.5 anti-TNF-α (BioLegend, #506322), BV421 anti-Granzyme B (BioLegend, #396414).

Cellular lipid peroxidation using BODIPY 581/591 C11

To evaluate the level of lipid peroxidation in tumor cells in mice, a single-cell suspension was first prepared. The cells were then stained with anti-CD45 antibody, followed by incubation with BODIPY 581/591 C11 (Invitrogen, #2770868) (2 μM) for 30 minutes. After washing three times with PBS, the samples were immediately analyzed by flow cytometry. The ratio of FITC (oxidized C11) mean fluorescence intensity (MFI) to PE (non-oxidized C11) MFI was calculated for each sample. Data were normalized to control samples, as shown for relative lipid ROS.

Enzyme-linked immunosorbent assay(ELISA)

First, peripheral blood or supernatant from fresh tumor tissue was collected from the mice and centrifuged at 1000g for 20 minutes at 4°C to remove debris and cells. Then, the concentration of IFN-γ was measured by mouse IFN-γ ELISA kit (Elabscience, E-EL-M0048) following the protocol provided by the manufacturer, and the actual concentration was calculated.

Western blotting

Cells were lysed in lysis buffer supplemented with 1 mM phenylmethylsulfonyl fluoride (PMSF) for 30min on ice. The cell lysates were boiled in SDS loading buffer for 15 minutes and then analyzed by SDS-PAGE (Bio-Rad). Subsequently, the samples were transferred onto polyvinylidene difluoride (PVDF) membranes. The membranes were blocked with 5% milk in PBST buffer (phosphate-buffered saline containing 0.05% Tween 20) for 1 hour, followed by incubation with primary antibodies overnight at 4 °C. After washing with PBST, the membranes were incubated with secondary antibodies for 1 hour and then washed three times with PBST. Signals were detected using enhanced chemiluminescence (ECL) (NCM Biotech, #P10300). The antibodies used in this study include: anti-GAPDH(Proteintech, #10013030), anti-GPX4 (Abcam, #ab125066).

Statistical analysis

All results are presented as the means ± SD. Comparisons between two groups were performed using an unpaired t-test, while comparisons among three and more groups were analyzed using one-way analysis of variance (ANOVA). Data were analyzed using GraphPad Prism v8.0.2 software. A p value < 0.05 was considered statistically significant (*p < 0.05; **p < 0.01; ***p < 0.001; ****p < 0.0001).

Declarations

Acknowledgments: Thank all those who supported and contributed to the study.

Funding: This study was supported by National Natural Science Foundation of China（82472799, 82172690 to L.L.; 82403814 to Y.G.）.

Author contributions: Conceptualization: Y.Z., Y.W. and L.L. Methodology: Y.Z., Y.C., Y.G., J.Z., Y.L., J.C. and Z.Q. Investigation: Y.Z. Formal analysis: Y.Z. and L.L. Validation: Y.Z and Y.C. Data curation: Y.Z. Project administration: Y.Z., Y.W. and L.L. Writing-original draft: Y.Z. and L.L. Writing-review and editing: Y.Z., Y.W. and L.L. Funding acquisition: L.L. and Y.G.

Competing interests: The authors declare no competing interests.

Data and materials availability: All data needed to evaluate the conclusions in the paper are present in the paper and/or the Supplementary Material.

References

1. Dixon SJ*, et al.* Ferroptosis: an iron-dependent form of nonapoptotic cell death. *Cell***149**, 1060-1072 (2012).
2. Stockwell BR. Ferroptosis turns 10: Emerging mechanisms, physiological functions, and therapeutic applications. *Cell***185**, 2401-2421 (2022).
3. Lei G, Zhuang L, Gan B. Targeting ferroptosis as a vulnerability in cancer. *Nature Reviews Cancer***22**, 381-396 (2022).

4. Nakamura T, Conrad M. Exploiting ferroptosis vulnerabilities in cancer. *Nature Cell Biology***26**, 1407-1419 (2024).
5. Ubellacker JM, Dixon SJ. Prospects for ferroptosis therapies in cancer. *Nature Cancer***6**, 1326-1336 (2025).
6. Hassannia B*, et al.* Nano-targeted induction of dual ferroptotic mechanisms eradicates high-risk neuroblastoma. *Journal of Clinical Investigation***128**, 3341-3355 (2018).
7. Xiao J*, et al.* Mitochondria-specific GPX4 inhibition enhances ferroptosis and antitumor immunity. *J Control Release***383**, 113841 (2025).
8. Wahida A, Conrad M. Decoding ferroptosis for cancer therapy. *Nature Reviews Cancer***25**, 910-924 (2025).
9. Maccarinelli F*, et al.* Iron supplementation enhances RSL3-induced ferroptosis to treat naïve and prevent castration-resistant prostate cancer. *Cell Death Discovery***9**, 81 (2023).
10. Wang W*, et al.* $CD8^+$ T cells regulate tumour ferroptosis during cancer immunotherapy. *Nature***569**, 270-274 (2019).
11. Zhou L*, et al.* Palmitoylation of GPX4 via the targetable ZDHHC8 determines ferroptosis sensitivity and antitumor immunity. *Nature Cancer***6**, 768-785 (2025).
12. Conche C*, et al.* Combining ferroptosis induction with MDSC blockade renders primary tumours and metastases in liver sensitive to immune checkpoint blockade. *Gut***72**, 1774-1782 (2023).
13. Shimasaki N, Jain A, Campana D. NK cells for cancer immunotherapy. *Nature Reviews Drug Discovery***19**, 200-218 (2020).
14. Vivier E, Rebuffet L, Narni-Mancinelli E, Cornen S, Igarashi RY, Fantin VR. Natural killer cell therapies. *Nature***626**, 727-736 (2024).
15. Zhang Y, Guo F, Wang Y. Hypoxic tumor microenvironment: Destroyer of natural killer cell function. *Chinese Journal of Cancer Research***36**, 138-150 (2024).
16. Böttcher JP*, et al.* NK Cells Stimulate Recruitment of cDC1 into the Tumor Microenvironment Promoting Cancer Immune Control. *Cell***172**, 1022-1037.e1014 (2018).
17. Bald T, Krummel MF, Smyth MJ, Barry KC. The NK cell–cancer cycle: advances and new challenges in NK cell–based immunotherapies. *Nature Immunology***21**, 835-847 (2020).
18. Li J*, et al.* Tumor-specific GPX4 degradation enhances ferroptosis-initiated antitumor immune response in mouse models of pancreatic cancer. *Science Translational Medicine***15**, eadg3049 (2023).
19. Xue Y*, et al.* Intermittent dietary methionine deprivation facilitates tumoral ferroptosis and synergizes with checkpoint blockade. *Nature Communications***14**, 4758 (2023).
20. Lin Y*, et al.* Histone deacetylase-mediated tumor microenvironment characteristics and synergistic immunotherapy in gastric cancer. *Theranostics***13**, 4574-4600 (2023).
21. Lang X*, et al.* Radiotherapy and Immunotherapy Promote Tumoral Lipid Oxidation and Ferroptosis via Synergistic Repression of SLC7A11. *Cancer Discovery***9**, 1673-1685 (2019).

22. Wolf NK, Kissiov DU, Raulet DH. Roles of natural killer cells in immunity to cancer, and applications to immunotherapy. *Nature Reviews Immunology***23**, 90-105 (2022).
23. Gocher AM, Workman CJ, Vignali DAA. Interferon-γ: teammate or opponent in the tumour microenvironment? *Nature Reviews Immunology***22**, 158-172 (2021).
24. Jin WJ*, et al.* NK cells propagate T cell immunity following in situ tumor vaccination. *Cell Reports***42**, (2023).
25. Bi J*, et al.* Checkpoint TIPE2 Limits the Helper Functions of NK Cells in Supporting Antitumor $CD8^+$ T Cells. *Advanced Science***10**, (2023).
26. Michelet X*, et al.* Metabolic reprogramming of natural killer cells in obesity limits antitumor responses. *Nature Immunology***19**, 1330-1340 (2018).
27. Rhode PR*, et al.* Comparison of the Superagonist Complex, ALT-803, to IL15 as Cancer Immunotherapeutics in Animal Models. *Cancer Immunology Research***4**, 49-60 (2016).
28. Liu B*, et al.* Evaluation of the biological activities of the IL-15 superagonist complex, ALT-803, following intravenous versus subcutaneous administration in murine models. *Cytokine***107**, 105-112 (2018).
29. Gao M*, et al.* Role of Mitochondria in Ferroptosis. *Molecular Cell***73**, 354-363.e353 (2019).
30. Liang D*, et al.* Ferroptosis surveillance independent of GPX4 and differentially regulated by sex hormones. *Cell***186**, 2748-2764.e2722 (2023).
31. Calhoon D*, et al.* Glycosaminoglycan-driven lipoprotein uptake protects tumours from ferroptosis. *Nature***644**, 799-808 (2025).
32. Poznanski SM*, et al.* Metabolic flexibility determines human NK cell functional fate in the tumor microenvironment. *Cell Metabolism***33**, 1205-1220.e1205 (2021).
33. Liao P*, et al.* $CD8^+$ T cells and fatty acids orchestrate tumor ferroptosis and immunity via ACSL4. *Cancer Cell***40**, 365-378.e366 (2022).
34. Wang C*, et al.* Reprogramming NK cells and macrophages via combined antibody and cytokine therapy primes tumors for elimination by checkpoint blockade. *Cell Reports***37**, 110021 (2021).
35. Kim K-S, Choi B, Choi H, Ko MJ, Kim D-H, Kim D-H. Enhanced natural killer cell anti-tumor activity with nanoparticles mediated ferroptosis and potential therapeutic application in prostate cancer. *Journal of Nanobiotechnology***20**, 428 (2022).
36. Sheppard S*, et al.* Fatty acid oxidation fuels natural killer cell responses against infection and cancer. *Proc Natl Acad Sci U S A***121**, e2319254121 (2024).

Figures

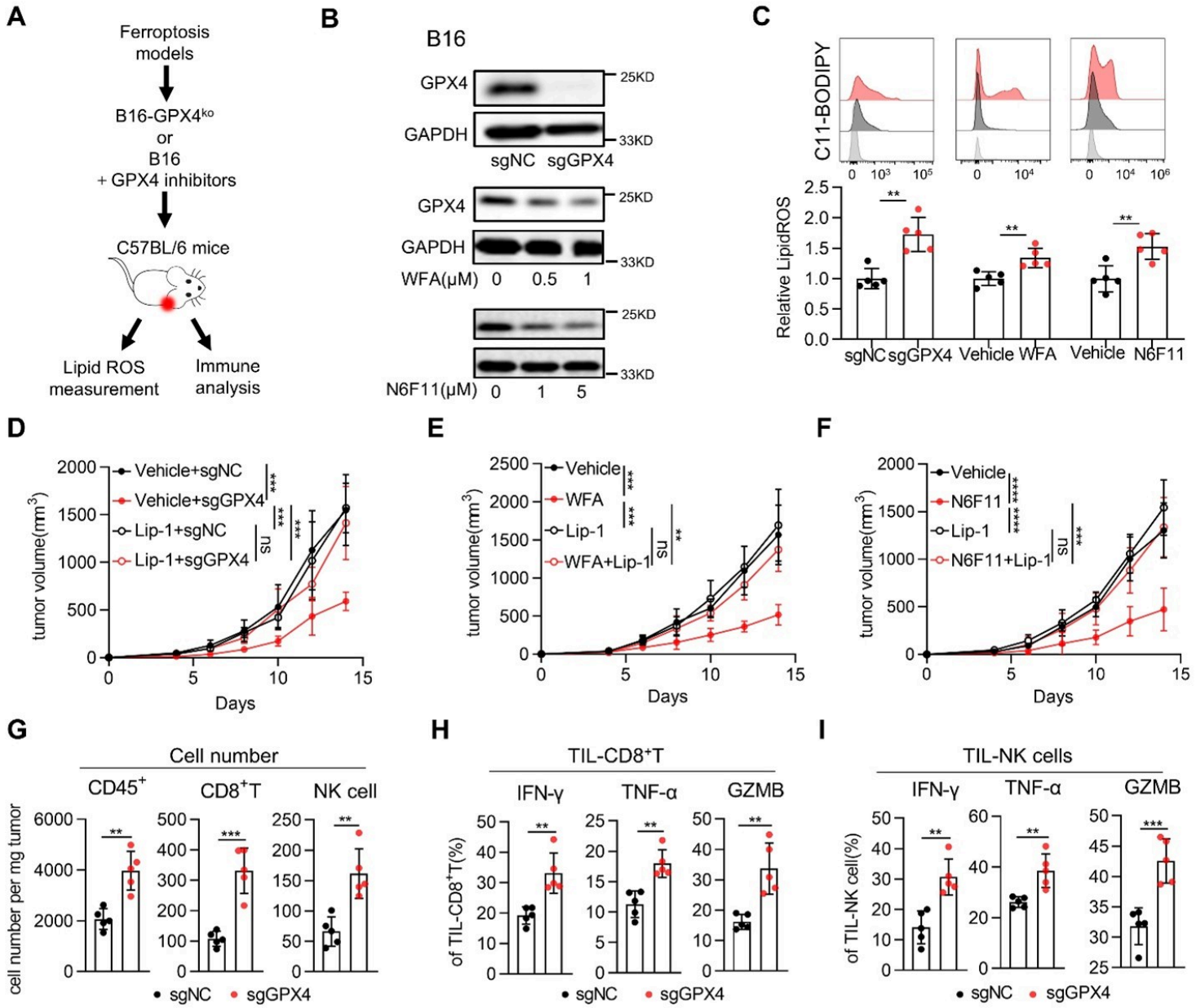


Figure 1

GPX4 inhibition triggers tumor ferroptosis and promotes anti-tumor immunity *in vivo*. (A) Experimental schematics of the effect of GPX4 knockout or inhibition on tumor ferroptosis and anti-tumor immunity *in vivo*. **(B)** Western blot confirming knockout of GPX4 by CRISPR-Cas9 or inhibition of GPX4 by WFA or N6F11 for 20h in B16. **(C)** Tumor lipid ROS in wild type B16(sgNC) or GPX4 knockout B16 (sgGPX4) tumors(left) in C57BL/6 mice, or in B16 tumors in C57BL/6 mice treated by WFA (or vehicle) (middle),or N6F11 (or vehicle) (right) (n = 5 mice).**(D)** Tumor growth of sgNC or sgGPX4 B16 tumors in C57BL/6 mice treated by Lip-1(n=5 mice). **(E and F)** Tumor growth of B16 tumors in C57BL/6 mice treated by WFA(E) or N6F11(F) in the presence or absence of Lip-1 (n=5 mice). **(G-I)** Tumor-infiltrating $CD45^+$, $CD8^+$ T, NK cells (G) and percentage of IFN-γ, TNF-α, GZMB of tumor-infiltrating $CD8^+$ T (TIL-$CD8^+$ T) cells (H) and tumor-infiltrating NK (TIL-NK) cells (I) in sgNC or sgGPX4 B16 tumors in C57BL/6 mice(n=5 mice). All mice were maintained on a normal chow diet containing vitamin E (60 IU/kg) throughout the

experiments. Statistical analysis was performed using unpaired t-test (C,G-I) and one-way analysis of variance (ANOVA) (D-F). Data represent the means ± SD. (**p 0.01, ***p 0.001, ****p 0.0001). ns, not significant.

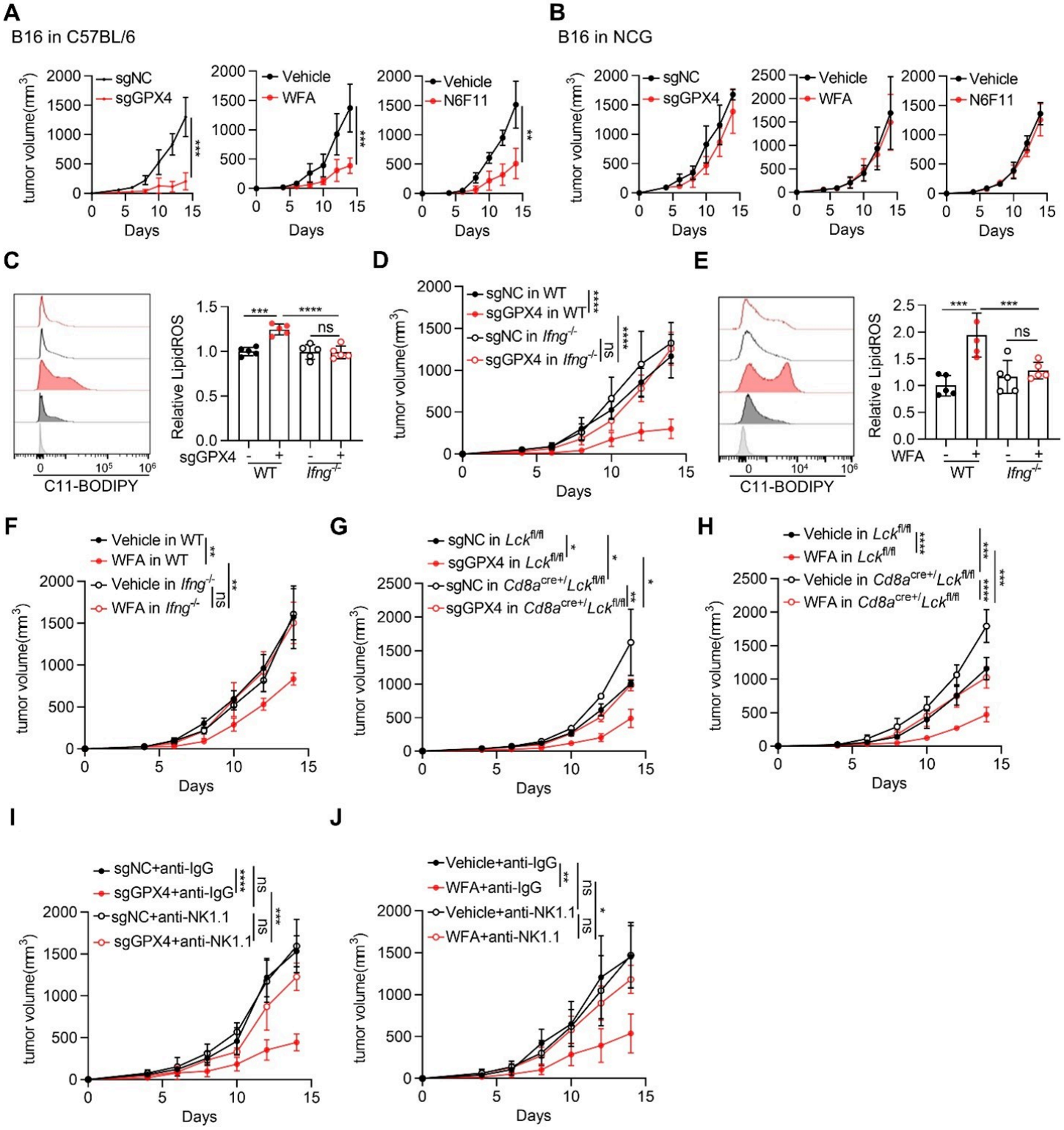


Figure 2

GPX4 inhibition requires NK cell-dependent immunity for tumor suppression *in vivo*. (A and B) Tumor growth of sgNC or sgGPX4 B16 tumors(left), or B16 tumors treated by WFA (middle),or N6F11 (right) in

C57BL/6 mice (A) or NCG mice (B) (n=5 mice). **(C)** Tumor lipid ROS in sgNC or sgGPX4 B16 tumors in WT mice or *Ifng*$^{-/-}$ mice(n=5 mice). **(D)** Tumor growth of sgNC or sgGPX4 B16 tumors in WT mice or *Ifng*$^{-/-}$ mice (n=5 mice). **(E)** Tumor lipid ROS in B16 tumors treated by WFA in WT mice or *Ifng*$^{-/-}$ mice (n=5 mice). **(F)** Tumor growth of B16 tumors treated by WFA in WT mice or *Ifng*$^{-/-}$ mice (n=5 mice). **(G)** Tumor growth of sgNC or sgGPX4 B16 tumors in *Lck*$^{fl/fl}$ mice or *Cd8a*$^{cre+/}$*Lck*$^{fl/fl}$ mice (n=5 mice). **(H)** Tumor growth of B16 tumors treated by WFA(or vehicle) in *Lck*$^{fl/fl}$ mice or *Cd8a*$^{cre+/}$*Lck*$^{fl/fl}$ mice (n=5 mice). **(I)** Tumor growth of sgNC or sgGPX4 B16 tumors in C57BL/6 mice with or without anti-NK1.1 antibody (n=5 mice). **(J)** Tumor growth of B16 tumors in C57BL/6 mice treated by WFA with or without anti-NK1.1 antibody (n=5 mice). All mice were maintained on a normal chow diet containing vitamin E (60 IU/kg) throughout the experiments. Statistical analysis was performed using unpaired t-test (A-B) and one-way analysis of variance (ANOVA) (C-J). Data represent the means ± SD. (*p□0.05, **p□0.01, ***p□0.001, ****p □0.0001). ns, not significant.

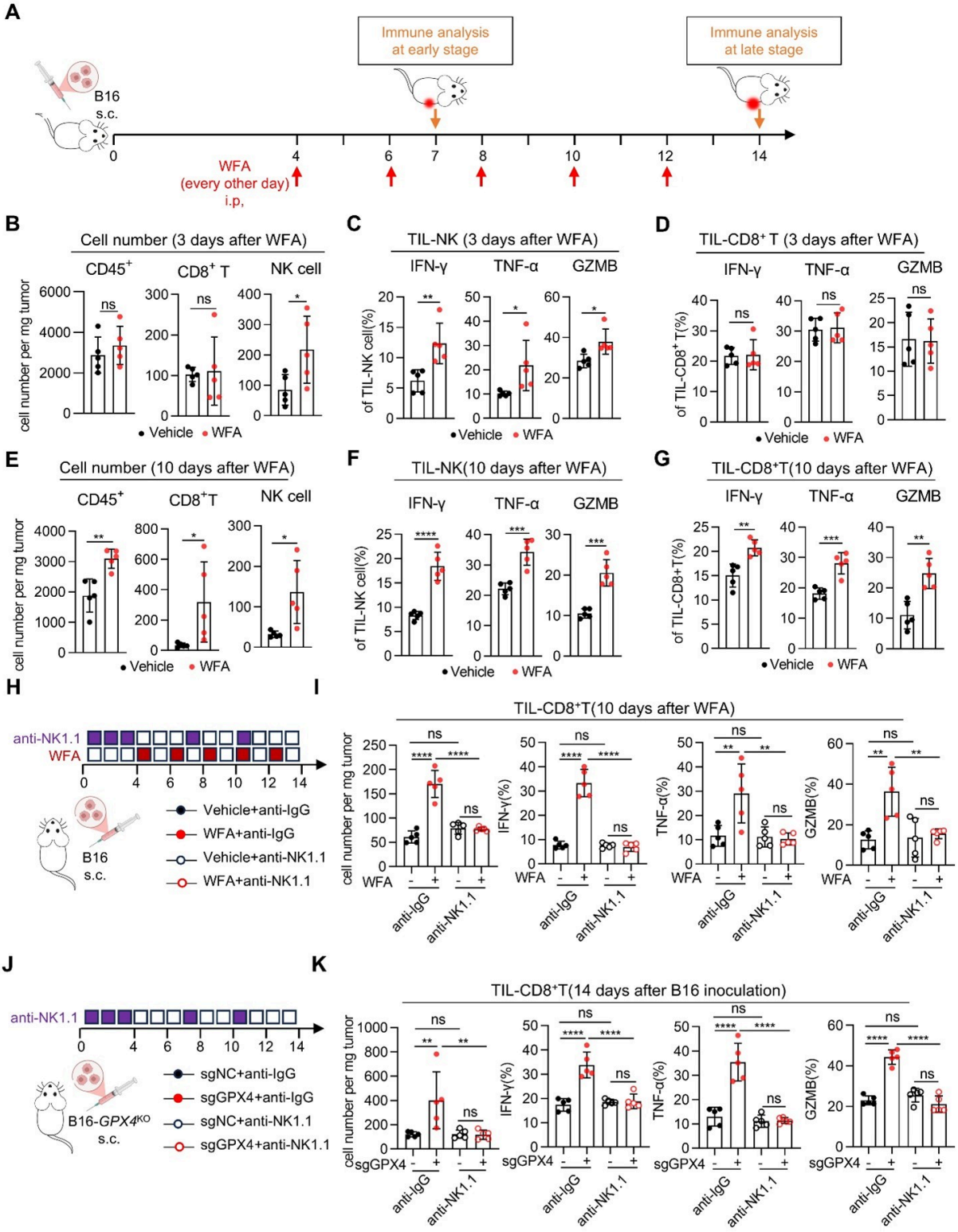


Figure 3

NK cell depletion abolishes GPX4 inhibition–induced CD8⁺ T cell activation. (A) Experimental schema to analyze tumor-infiltrating immune cells at early and late stages treated by WFA (or vehicle) in B16 models. **(B-D)** Tumor-infiltrating CD45$^+$, CD8$^+$ T, NK cells (B) and percentage of IFN-γ, TNF-α, GZMB of tumor-infiltrating NK (TIL-NK) cells (C) and tumor-infiltrating CD8$^+$ T (TIL-CD8$^+$ T) cells (D) at day3

following WFA treatment (n=5 mice). **(E-G)** Tumor-infiltrating $CD45^+$, $CD8^+$ T, NK cells (E) and percentage of IFN-γ, TNF-α, GZMB of TIL-NK cells (F) and TIL-$CD8^+$ T cells (G) at day10 following WFA treatment (n=5 mice).**(H)** Experimental schema to analyze effect of NK cells depletion by anti-NK1.1 antibody on TIL-$CD8^+$ T cells in B16 models treated by WFA. **(I)** Infiltration and percentage of IFN-γ, TNF-α, GZMB of TIL-$CD8^+$ T cells at day10 following WFA treatment in B16 models treated by anti-NK1.1 antibody (n=5 mice). **(J)** Experimental schema to analyze effect of NK cells depletion by anti-NK1.1 antibody on TIL-$CD8^+$ T cells in sgNC or sgGPX4 B16 models. **(K)** Infiltration and percentage of IFN-γ, TNF-α, GZMB of TIL-$CD8^+$ T cells at day14 following sgNC or sgGPX4 B16 cells inoculation treated by anti-NK1.1 antibody (n=5 mice). All mice were maintained on a normal chow diet containing vitamin E (60 IU/kg) throughout the experiments. Statistical analysis was performed using unpaired t-test (B-G) and one-way analysis of variance (ANOVA) (I, K). Data represent the means ± SD. (*p□0.05, **p□0.01,***p□0.001, ****p□0.0001). ns, not significant.

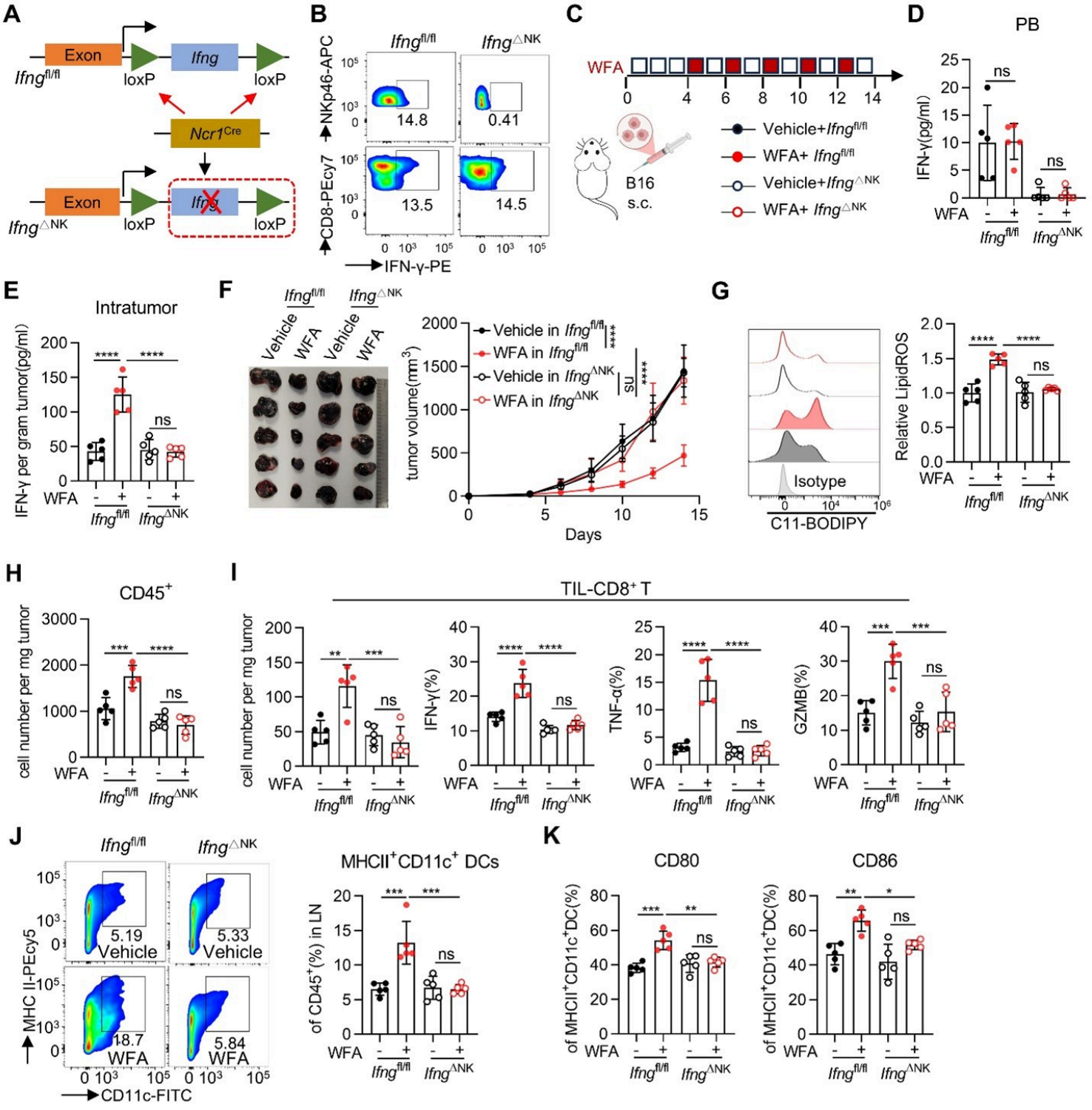


Figure 4

NK cell-derived IFN-γ orchestrates dendritic cell activation and adaptive immune priming in response to GPX4 inhibition. (A) Schematic diagram of conditional IFN-γ knockout in NK cells in C57BL/6 mice. **(B)** Representative plots showing the expression of IFN-γ on $CD45^+$ $CD3^-$ $NKp46^+$ and $CD45^+$ $CD3^+$ $CD8^+$ cells from *Ifng*$^{fl/fl}$ mice and *Ifng*$^{\triangle NK}$ mice spleen cells. **(C)** Experimental schema of B16 model in *Ifng*$^{fl/fl}$ mice and *Ifng*$^{\triangle NK}$ mice treated by WFA. **(D and E)** Quantification of IFN-γ level in peripheral blood (PB) (D)

or tumor supernatant (E) among B16-bearing *Ifng*$^{fl/fl}$ mice and *Ifng*$^{\triangle NK}$ mice at day10 following WFA treatment (n=5 mice). **(F)** Tumor growth of B16 tumors in *Ifng*$^{fl/fl}$ mice and *Ifng*$^{\triangle NK}$ mice treated by WFA (n=5 mice). **(G)** Tumor lipid ROS in B16 tumors treated by WFA in *Ifng*$^{fl/fl}$ mice and *Ifng*$^{\triangle NK}$ mice. **(H)** Infiltration of CD45^{+} cells at day10 following WFA treatment (n=5 mice). **(I)** Infiltration and percentage of IFN-γ, TNF-α, GZMB of tumor-infiltrating CD8^{+} T (TIL-CD8^{+} T) cells at day10 following WFA treatment (n=5 mice). **(J and K)** Flow cytometric analysis of abundance of MHCII^{+}CD11c^{+} DCs (J) and expression of CD80, CD86 on MHCII^{+}CD11c^{+} DCs. (K) in tumor-draining lymph nodes at day10 following WFA treatment (n=5 mice). All mice were maintained on a normal chow diet containing vitamin E (60 IU/kg) throughout the experiments. Statistical analysis was performed using one-way analysis of variance (ANOVA) (D-K). Data represent the means ± SD. (*p□0.05, **p□0.01,***p□0.001, ****p□0.0001). ns, not significant.

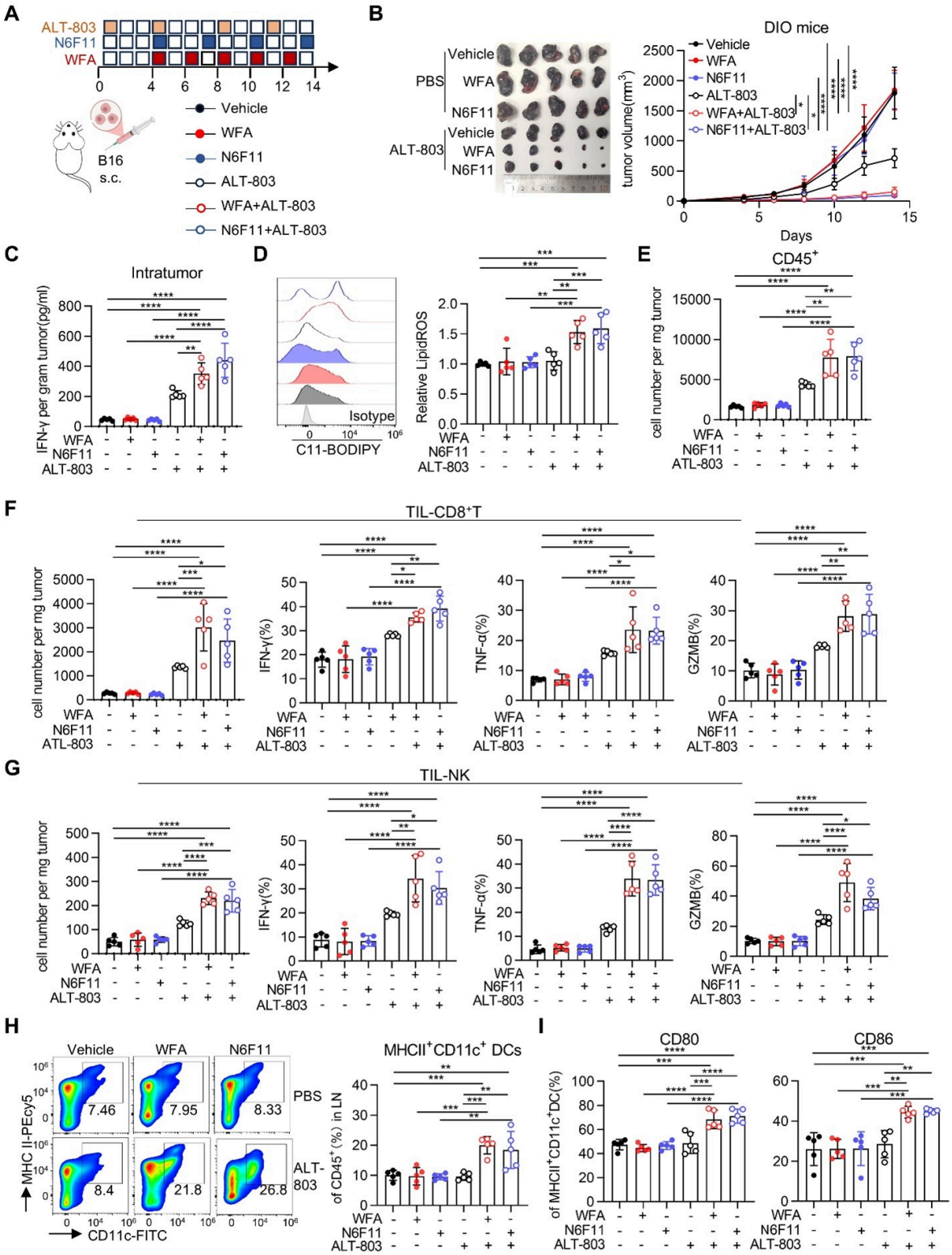


Figure 5

Restoring NK cell function overcomes obesity associated resistance to GPX4 inhibition driven tumor ferroptosis and immunity. (A) Experimental schema of B16 model treated by GPX4 inhibitors (WFA or N6F11) with or without ALT-803 in diet-induced obesity (DIO) mice. **(B)** Tumor growth of B16 tumors treated by WFA or N6F11 with or without ALT-803 in DIO mice (n=5). **(C)** Quantification of IFN-γ level in tumor supernatant at day14 following tumor inoculation in DIO mice (n=5). **(D)** Tumor lipid ROS at day14

following tumor inoculation in DIO mice (n=5). **(E)** Infiltration of $CD45^+$ cells at day14 following tumor inoculation in DIO mice (n=5). **(F)** Infiltration and percentage of IFN-γ, TNF-α, GZMB of tumor-infiltrating $CD8^+$ T (TIL-$CD8^+$ T) cells at day14 following tumor inoculation in DIO mice (n=5). **(G)** Infiltration and percentage of IFN-γ, TNF-α, GZMB of tumor-infiltrating NK (TIL-NK) cells at day14 following tumor inoculation in DIO mice (n=5). **(H and I)** Flow cytometric analysis of abundance of $MHCII^+CD11c^+$DCs (H) and expression of CD80, CD86 on $MHCII^+CD11c^+$ DCs (I) in tumor-draining lymph nodes at day14 following tumor inoculation in DIO mice (n=5). All mice were maintained on a high-fat diet containing vitamin E (60 IU/kg) throughout the experiments. Statistical analysis was performed using one-way analysis of variance (ANOVA) (B-I). Data represent the means ± SD. (*p□0.05, **p□0.01,***p□0.001, ****p□0.0001). ns, not significant.